Plasmon-Enhanced Upconversion Luminescence in Single Nanophosphor–Nanorod Heterodimers Formed through Template-Assisted Self-Assembly

Nicholas J. Greybush,[†] Marjan Saboktakin,[‡] Xingchen Ye,[§] Cristian Della Giovampaola,[‡] Soong Ju Oh,[†] Nathaniel E. Berry,[†] Nader Engheta,[†,‡,∥,⊥] Christopher B. Murray,[*,†,§] and Cherie R. Kagan[*,†,‡,§]

[†]Department of Materials Science and Engineering, [‡]Department of Electrical and Systems Engineering, [§]Department of Chemistry, [∥]Department of Physics and Astronomy, and [⊥]Department of Bioengineering, University of Pennsylvania, Philadelphia, Pennsylvania 19104, United States

ABSTRACT We demonstrate plasmonic enhancement of upconversion luminescence in individual nanocrystal heterodimers formed by template-assisted self-assembly. Lithographically defined, shape-selective templates were used to deterministically coassemble single Au nanorods in proximity to single hexagonal (β-phase) $NaYF_4$:Yb^{3+}, Er^{3+} upconversion nanophosphors. By tailoring the dimensions of the rods to spectrally tune their longitudinal surface plasmon resonance to match the 977 nm excitation wavelength of the phosphors and by spatially localizing the phosphors in the intense near-fields surrounding the rod tips, several-fold luminescence enhancements were achieved. The enhancement effects exhibited a strong dependence on the excitation light's polarization relative to the rod axis. In addition, greater enhancement was observed at lower excitation power densities due to the nonlinear behavior of the upconversion process. The template-based coassembly scheme utilized here for plasmonic coupling offers a versatile platform for improving our understanding of optical interactions among individual chemically prepared nanocrystal components.

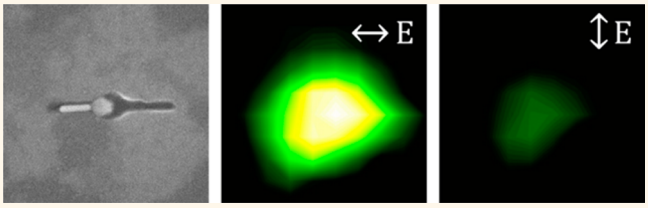

KEYWORDS: upconversion nanocrystals · template-assisted self-assembly · plasmon-enhanced luminescence · single particle · gold nanorod · polarization dependence

Upconversion phosphors are an attractive class of materials with the ability to absorb low-energy light and re-emit light having higher energy.[1−8] This property has made spectral upconverters attractive for a number of applications including photovoltaics,[9−12] bioimaging and therapy,[13−17] solid-state lighting,[18] and display technologies.[19,20] For example, solar cell efficiency could be improved by extending the usable portion of the solar spectrum by upconverting sub-bandgap infrared light that is otherwise lost. As contrast agents in biological systems, upconverters enable the use of low-power, infrared excitation, which offers reduced autofluorescence background while penetrating more deeply and with less damage to tissue. While developments in these application areas are promising, widespread implementation of upconversion materials remains limited by the low efficiency of the upconversion process. Even for the most effective materials, such as hexagonal (β) phase $NaYF_4$ nanocrystals codoped with Yb^{3+} and Er^{3+}, the quantum yield is often below 1%,[21−23] motivating the development of routes to enhance upconversion luminescence.

One approach to enhance upconversion is to explore chemical design strategies such as tailoring the doping level, host material and phase, and nanocrystal morphology.[24−29] An alternative, parallel strategy involves enhancing the luminescence of phosphors through coupling to plasmonic nanostructures. The collective oscillations of conduction electrons within nanoscale metal structures, known as surface plasmon resonances (SPRs), can greatly amplify the luminescence from nearby emitters,[30] as extensively demonstrated for

* Address correspondence to kagan@seas.upenn.edu, cbmurray@sas.upenn.edu.

Received for review July 6, 2014 and accepted September 2, 2014.

Published online September 02, 2014
10.1021/nn503675a

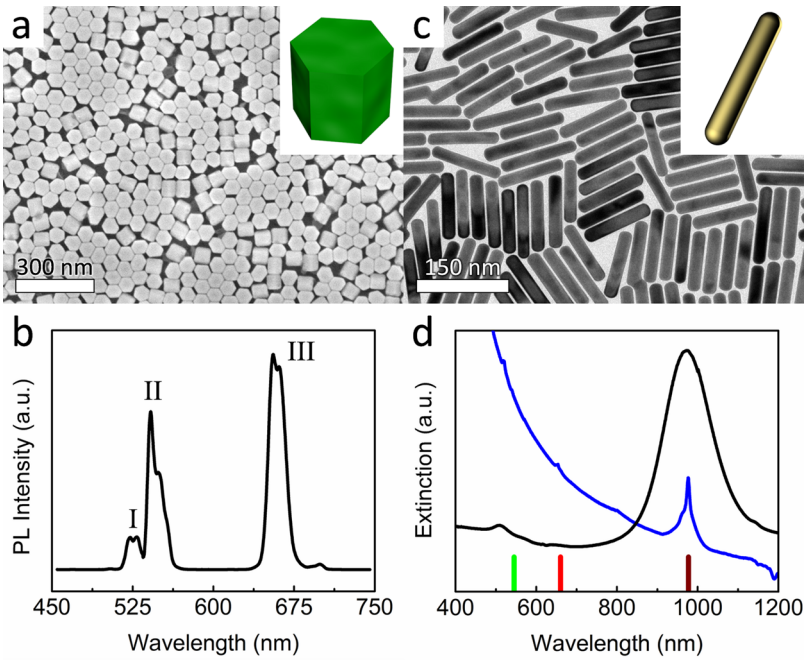

Figure 1. (a) SEM image of $NaYF_4$:Yb^{3+},Er^{3+} UCNPs. Inset: Schematic depiction of hexagonal prismatic UCNP morphology. (b) Emission spectrum of UCNPs under 977 nm excitation. Peak labels indicate the (I) $^2H_{11/2} \rightarrow {}^4I_{15/2}$, (II) $^4S_{3/2} \rightarrow {}^4I_{15/2}$, and (III) $^4F_{9/2} \rightarrow {}^4I_{15/2}$ transitions of Er^{3+}. (c) TEM image of Au NRs. Inset: Schematic depiction. (d) Extinction spectra of Au NRs (black) and UCNPs (blue). Vertical lines denote the 977 nm excitation (dark red), 660 nm UCNP emission (red), and 545 nm UCNP emission (green).

semiconductor quantum dot[31−33] and single-molecule[34−36] fluorescence. A number of recent reports have explored plasmonic enhancement of upconversion nanophosphors (UCNPs) with strategies including assembling UCNPs with Au and Ag nanoparticles,[37−42] placing UCNPs near structured metal surfaces,[43−49] and employing core−shell architectures with either plasmonic cores[50,51] or shells.[52−57] However, single-particle optical studies of UCNPs[8,58−61] and their plasmon-enhanced luminescence[38,52,57] remain limited. Single-particle measurements are valuable in complementing studies on ensembles of UCNPs, as ensemble heterogeneities in the upconverting and plasmonic components and in their spatial arrangement can obscure the underlying physics of their coupling. The sensitivity of luminescence enhancement to design parameters is more easily uncovered using single-particle experiments, enabling the optimization of a model unit structure that can be extended to a useful large-scale system.

Single-particle studies of plasmon-coupled UCNPs require a robust means to precisely assemble a desired structure for optical characterization. While previous experiments have used, for example, manual manipulation of individual nanocrystals with an atomic force microscope (AFM) tip,[38] a method to self-assemble predesigned structures with controlled orientation is highly advantageous. Template-assisted self-assembly[62,63] fulfills this need by combining the design freedom of lithography with the highly parallel nature of self-assembly. In this approach, chemically synthesized components are made to assemble within topographical features defined on a substrate by lithography. This technique has been used to successfully assemble micron-[62−65] and nanosized[43,63,66−77] particles for applications including plasmonics,[73,74,76,77] surface-enhanced Raman scattering,[68] and nanoelectronics[75] and was recently employed for the placement of UCNPs into gold nanohole arrays for luminescence enhancement.[43] In the present work, we utilize template-assisted self-assembly to form discrete nanocrystal heterodimers consisting of a single UCNP and a single gold nanorod (Au NR). These individual unit structures are assembled in well-defined locations and orientations on the substrate, enabling us to investigate the magnitude of plasmonic enhancement by studying the polarization- and power-dependent luminescence properties of individual UCNPs in the presence and absence of Au NRs.

RESULTS AND DISCUSSION

The nanocrystal building blocks used in our study are shown in Figure 1. We synthesized UCNPs composed of hexagonal (β) phase $NaYF_4$ codoped with Yb^{3+} and Er^{3+} that are hexagonal prismatic in shape with an average height of 61 nm ± 5% and face diagonal of 66 nm ± 4% (Figure 1a). In this UCNP system, incident light at 977 nm resonantly excites the $^2F_{7/2} \rightarrow {}^2F_{5/2}$ transition in Yb^{3+}, and this energy is subsequently transferred nonradiatively to nearby Er^{3+} ions through a series of energy transfer and phonon relaxation steps to populate the emitting states of Er^{3+}, as shown in Supporting Information Figure S1. The visible emission spectrum (Figure 1b) displays three

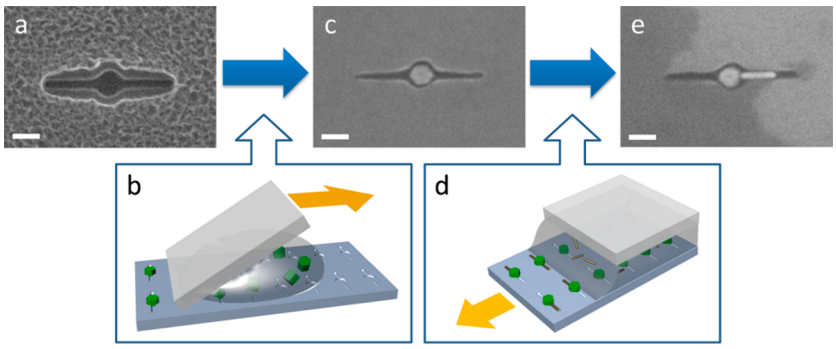

Figure 2. (a) Representative SEM image of an empty template defined in SiO_2 (with resist layer visible). (b) Schematic depiction of UCNP assembly *via* a "squeegee method" in which a polymer wiper sweeps the UCNP solution across the substrate. Not to scale; the UCNPs and template features are enlarged for clarity. (c) SEM image of a single UCNP in a template (after ALD deposition of the SiO_2 overcoat). (d) Schematic of Au NR assembly with an assembly apparatus in which the substrate moves relative to a fixed slide that restrains the Au NR solution. Not to scale. (e) SEM image of a UCNP and Au NR heterodimer structure formed inside the template. Scale bars for SEM: 100 nm.

major upconversion emission bands centered around (I) 525, (II) 545, and (III) 660 nm, corresponding to transitions from the $^2H_{11/2}$, $^4S_{3/2}$, and $^4F_{9/2}$ states to the $^4I_{15/2}$ ground state of Er^{3+}, respectively. Au NRs were synthesized with an average length of 109 nm ± 8% and width of 20 nm ± 9% (Figure 1c). This Au NR aspect ratio was targeted specifically so that the broad SPR spectrally overlaps the UCNP excitation. Figure 1d illustrates that the main spectral feature in the Au NR extinction around 975 nm, the longitudinal SPR resulting from excitation along the long axis of the rod, coincides with the $^2F_{7/2} \rightarrow {}^2F_{5/2}$ absorption in Yb^{3+} as desired.

This spectral overlap is critical in determining the nature, if any, of plasmonic luminescence enhancement. In general, the presence of a plasmonic structure can affect the luminescence of a nearby emitter in two ways.[78] First, the highly concentrated electric fields surrounding the plasmonic structure can increase the excitation rate of the emitter. Second, the quantum yield of the emitter can also be modified to enhance (or quench) the emission. Excitation and quantum yield enhancement are sensitive, respectively, to the spectral overlap of the plasmon resonance with the excitation and the emission wavelengths of the luminophore.[79,80] In our system, we therefore are targeting excitation enhancement and expect limited contribution from quantum yield enhancement.

In addition to spectral overlap, effective plasmon-enhanced excitation requires spatial localization of the UCNP within the enhanced near-fields surrounding the plasmonic structure. We therefore employed a template-assisted self-assembly technique to generate spatially well-defined pairs of UCNPs and Au NRs, as illustrated in Figure 2. First, a series of short trenches was patterned in SiO_2 on a silicon substrate by electron-beam lithography and reactive ion etching. The shape of these topographical templates was finely tuned so that the central portion could only accept one UCNP per template and that the extended arms of the template were suitable for accepting individual Au NRs. The SEM image in Figure 2a shows a representative template structure following resist development and etching. To assemble the UCNPs into the templates, we employed a "squeegee method" previously demonstrated by our group for the assembly of UCNPs.[43,81] As pictured schematically in Figure 2b, a drop of UCNPs in hexanes was placed on the templated area and then swept across the surface using a flexible piece of polydimethylsiloxane (PDMS), driving the UCNPs at the liquid meniscus downward into the depressions. The resist layer was then removed, clearing away any UCNPs deposited nonspecifically outside the templates. Next, a thin (6 nm) layer of SiO_2 was deposited on the surface using atomic layer deposition (ALD). This layer served a dual purpose: (1) it prevented the Au NRs from approaching too closely to the phosphor and quenching the emission,[37] and (2) it secured the UCNPs in place while the Au NRs were being assembled. A representative SEM image of a single-phosphor structure after ALD is shown in Figure 2c.

While the squeegee method was effective for the assembly of UCNPs dispersed in alkanes, the Au nanorods were dispersed in water, and matching the rate of manual translation of the PDMS wiper with the slow water evaporation rate was more challenging. However, recent successful demonstrations of Au NR templated assembly using capillary action[66,71,72] motivated us to construct our own home-built apparatus (Figure 2d) to use this approach for Au NR assembly. Briefly, a dispersion of Au NRs was sandwiched between a fixed glass slide and the substrate, which was mounted on a linear translation stage. As the substrate was slowly moved relative to the fixed slide, the meniscus of the Au NR solution was drawn across the templates, and capillary force directed the rods into their intended positions adjacent to the UCNPs. Figure 2e shows a representative SEM image of a rod−phosphor dimer formed using this assembly

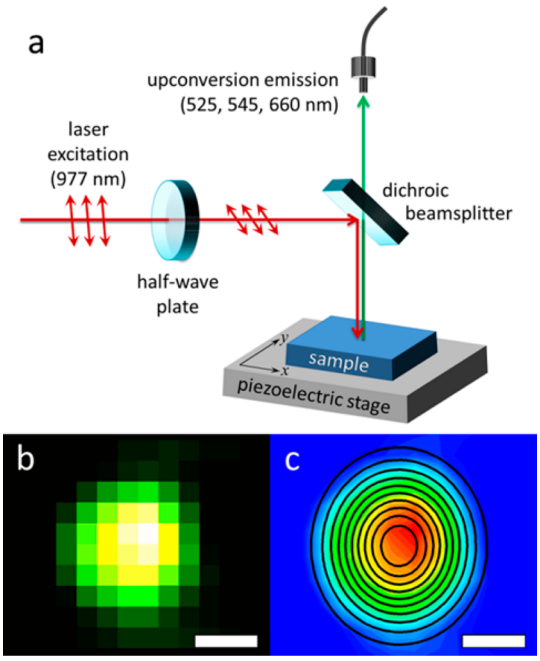

Figure 3. (a) Schematic of the PL mapping setup. (b) Spatial map of PL from a single UCNP−NR heterodimer structure. Pixel brightness indicates spectrally integrated PL intensity. (c) Two-dimensional Gaussian fit (black contours) superimposed over a contour map of the data in (b). Scale bars in (b) and (c) are 500 nm.

method. Additional SEM images are provided in Supporting Information Figure S2. For the heterodimers selected for photoluminescence measurements, the average distance from the rod tip to the UCNP was 14 ± 5 nm. While we are still optimizing the capillary assembly of nanocrystals in our lab, our coassembly scheme successfully demonstrates shape-selective assembly wherein nanocrystal components are directed with high specificity into template features corresponding to their size and aspect ratio.

The photoluminescence (PL) of the UCNPs and the UCNP−NR heterodimers was studied by scanning, confocal, PL microscopy using the setup depicted in Figure 3a. The sample was mounted on the piezoelectric translation stage of an optical microscope and rastered in two dimensions under a diffraction-limited 977 nm laser excitation spot focused by the microscope objective. The upconverted emission was collected by the objective, transmitted through a dichroic beamsplitter that filtered out reflected excitation light, and focused onto an optical fiber that carried the light to a spectrometer coupled with a CCD camera for detection. Importantly, a half-wave plate in the laser beam path allowed us to orient the laser's linear polarization direction along either the Au NR's long or short axis. The laser power was maintained at a desired constant value for the duration of a measurement by a feedback loop that sampled the beam power and automatically adjusted the laser output *via* rotation of a gradient neutral density filter.

By measuring the PL at each point in the raster, spatial maps of PL intensity could be generated, as shown in Figure 3b. In this representation, the color intensity of each pixel indicates the total detected PL, spectrally integrated over all three major emission bands at 525, 545, and 660 nm. Because of the small size of the diffraction-limited laser spot (~1.5 μm diameter) relative to the separation between individual structures on the substrate (~13.5 μm), PL maps of individual single-phosphor and rod−phosphor structures could be acquired. While the structures themselves were too small to be resolved in the optical microscope, alignment marks patterned in the periphery allowed specific structures to be located and mapped after their characterization by SEM. The PL maps were fit to a 2D Gaussian function (Figure 3c) whose height was used to quantify the PL intensity for a given measurement.

PL measurements were taken for several examples each of single-phosphor and rod−phosphor structures to generate statistics of the luminescence enhancement. A representative PL map for each structure measured is provided in Supporting Information Figure S3. Figure 4a presents the inverse-variance weighted average value of PL intensity for these two structure types under longitudinally and transversely oriented laser excitation with a power density of 1.6×10^6 W/cm^2. The presence of the Au NR was found to enhance the luminescence intensity by factors of 1.9 and 1.5 for the longitudinal and transverse polarizations, respectively. Figure 4b shows measurements of the same structures when the laser power was reduced by a factor of 10 to 1.6×10^5 W/cm^2. In the low-power case, enhancement factors of 2.5 for longitudinal and 1.4 for transverse polarization were observed. It is important to note that these measurements encompass variations among samples in phosphor and rod size and in their separation, as discussed in more detail below.

As expected, the single phosphors without Au NRs demonstrated little sensitivity to the laser polarization. However, for rod−phosphor heterodimers, the longitudinal polarization resulted in greater PL intensity than the transverse polarization. This comparison is presented more explicitly in Figure 4c,d, which shows the ratio between PL for excitation with longitudinal laser polarization and PL for excitation with transverse polarization for each of the rod−phosphor and single-phosphor structures studied. The polarization ratio can be used as a metric for luminescence enhancement by anisotropic structures like nanorods where the enhancement along one direction is expected to be small.[82] As shown in our simulations below, there is no excitation enhancement predicted in the transverse case. From an experimental perspective, constructing this ratio is a very direct comparison, as the PL intensity was measured for each polarization in immediate succession at each point in the raster before the stage

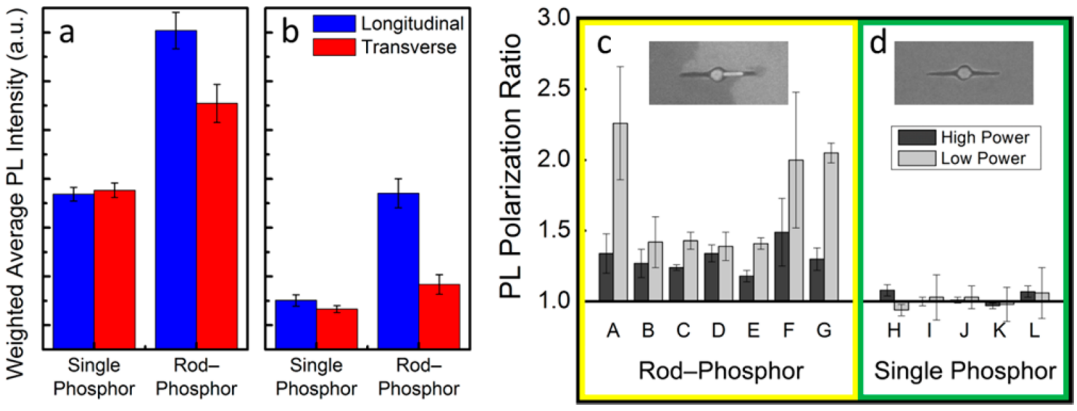

Figure 4. Inverse-variance weighted average PL intensity for single-phosphor and rod−phosphor structures under longitudinal and transverse laser polarization for power densities of (a) 1.6 × 10^6 W/cm^2 and (b) 1.6 × 10^5 W/cm^2. Error bars represent one standard deviation. (c,d) Ratio between PL from longitudinal excitation and transverse excitation for various (c) rod−phosphor (A−G) and (d) single-phosphor (H−L) structures (representative SEM images inset). High and low power refer to the same power densities as (a) and (b). Error bars represent one standard deviation over at least three measurements for low-power and two for high-power excitation.

was translated to the next pixel in the map. As seen in Figure 4c, the PL polarization ratio was always greater than unity for the rod−phosphor cases, with magnitudes of up to ~2.3 for one of the structures. Again, the single phosphors demonstrated no polarization sensitivity, having PL polarization ratios near unity (Figure 4d). Consistent with the expectation that the polarization-dependent enhancement arises from excitation (rather than emission) enhancement, when integrated separately, the red and green PL bands displayed similar polarization ratios (Supporting Information Figure S4).

The luminescence enhancement is also observed by comparing the PL spectra under each polarization for the single phosphors and for the rod−phosphor heterodimers. As expected, there was no difference between the two polarizations in the single-phosphor case, as shown in the representative spectra of Figure 5a. However, Figure 5b illustrates that for the rod−phosphor heterodimers, in addition to an increase in intensity, the PL spectrum for the longitudinal polarization exhibits several spectral changes. Most prominently, the finer spectral structure in peak II evolves, with the ratio of the peak height at 556 nm to that at 541 nm increasing substantially. As shown in the power-dependent PL spectra for UCNP ensembles (Supporting Information Figure S5), and in agreement with the literature,[8] the relative emergence of the 556 nm peak (as well as of smaller peaks at 469 and 504 nm) is a signature of increased excitation power. To rule out the possibility that this peak arises at high power in the ensemble measurements due to local sample heating, PL spectra were collected as a function of temperature at a constant laser power. Changes in the shape of the spectra in this region were negligible up to the highest temperature measured (440 K). Therefore, it is likely that the 556 nm signature appears for the rod−phosphor structure under longitudinal

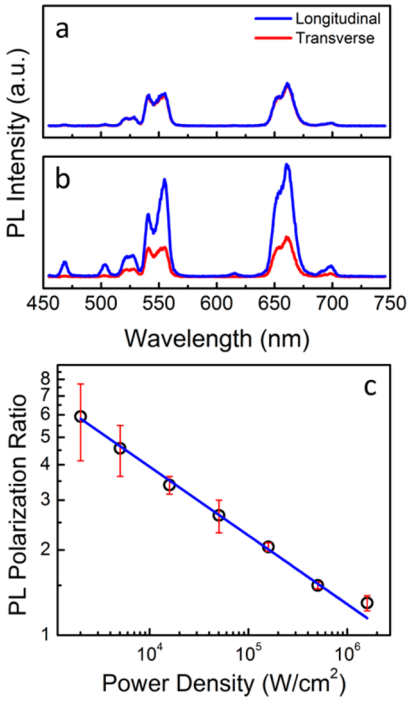

Figure 5. (a,b) Representative PL spectra from the center of the phosphor under longitudinal (blue) and transverse (red) incident polarization for (a) a single phosphor and (b) a rod−phosphor heterodimer. Each set of curves was normalized so that the transverse curves are of equal height for comparison. Excitation power density was 1.6 × 10^5 W/cm^2. (c) PL polarization ratio *versus* excitation power density (log scales) with fit to eq 1 (blue). Error bars are one standard deviation.

polarization because of the increased local field intensity due to the plasmon resonance.

For all of the rod−phosphor heterodimers studied in Figure 4c, the polarization sensitivity was more pronounced for the low-power excitation. To investigate this trend further, the PL polarization ratio for sample "G" was measured at additional excitation power levels ranging over nearly 3 orders of magnitude from the

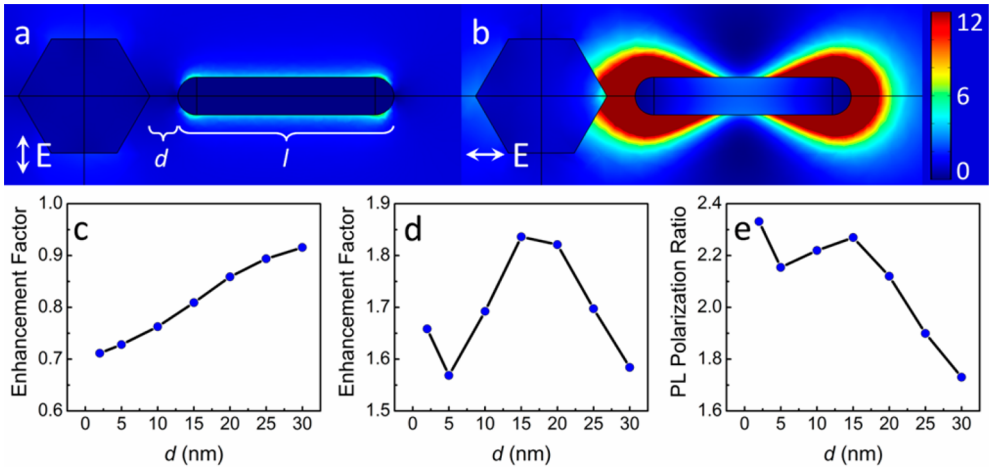

Figure 6. Simulated field intensity enhancement maps for (a) transverse and (b) longitudinal excitation polarization. (c,d) Simulated PL enhancement factor as a function of rod−phosphor separation *d* for (c) transverse and (d) longitudinal polarization. (e) Simulated PL polarization ratio as a function of rod−phosphor separation *d*.

previous "high-power" value of 1.6×10^6 W/cm^2 down to 2.0×10^3 W/cm^2. As seen in Figure 5c, the PL polarization ratio increased up to a value of ~6 as the incident power was decreased. The trend of increased PL polarization ratio at lower power was also consistently observed in other rod−phosphor structures, as shown in Supporting Information Figure S6. The power dependence of PL enhancement is explained by first considering the underlying power dependence of the upconversion process. Upconversion luminescence has been observed to scale with power P as P^n.[83] While in the low-power limit n is constant and equal to 2 (the number of photons in the upconversion process), as power is increased, the value of n can itself be power-dependent.[84] This behavior can be observed in a plot of log(PL) *versus* log(P), where the slope indicates the value of n. As shown in Supporting Information Figure S7, over the range of powers used in our study, this slope decreased from 1.3 to 0.4 as power was increased. To account for this behavior, we use a modified power law of the form $PL = kP^{C\cdot\log(P)+B}$, where k, C, and B are fitting parameters. With $y = \log(PL)$ and $x = \log(P)$, the shape of the log−log plot is then represented by the parabola $y = \log(k) + Bx + Cx^2$, which expresses the upconversion saturation seen at the high power levels applicable in single-particle experiments. In addition to our data, experimental and simulation results in the literature[8] could also be fit to the modified power law of this form. The PL polarization ratio can then be calculated as a function of incident laser power. Because the PL enhancement is due to an increase in the local field intensity surrounding the Au NR, we can introduce a field enhancement factor F such that $F\cdot P$ represents the increased local power experienced by the phosphor under longitudinal polarization. The longitudinal-to-transverse PL polarization ratio can then be written using the explicit form of the phosphor power dependence as

$$\frac{[F\cdot P]^{C\cdot\log(F\cdot P)+B}}{[P]^{C\cdot\log(P)+B}} \quad (1)$$

Figure 5c shows the very good agreement of the experimental data with this prediction. The linear relationship between log(PL polarization ratio) and log(power density) is shown explicitly in Supporting Information Supplemental Discussion 1. While the limited PL signal associated with single-particle measurements prevented investigating even lower power densities, it may be expected that the enhancement will continue to rise as the power law exponent approaches the low-power limit $n = 2$.

To better understand the magnitude and sample-to-sample variation of PL enhancement in the UCNP−NR heterodimers, we performed simulations using COMSOL Multiphysics software of the polarization-dependent PL of the phosphors with and without the Au NRs and as a function of the experimentally observed variation in rod size and rod−phosphor separation. Spatial maps of the field intensity enhancement under 977 nm excitation, defined as the ratio of the electric field intensity with and without the nanorod, were generated for each incident polarization, as shown in Figure 6a,b. It is clear that the longitudinal polarization results in amplified field intensity near the rod tip where the phosphor is located, in contrast to the absence of enhancement for transverse polarization. Due to the spatial distribution of the field intensity, different regions of the phosphor volume experience different amounts of enhancement under longitudinal excitation. To explore this variation, the field intensity enhancement was evaluated at six representative points (locations shown in Supporting Information Figure S8). For each of the six points, the field intensity enhancement decreases with increasing rod−phosphor separation distance d (Supporting Information Figure S9), and as expected from the shape of the field distribution,

points nearest the rod tip are most strongly impacted while those further away feel more limited effects.

In addition to the field enhancement, quenching due to losses in the nanorod must also be taken into consideration. This is done by calculating the emission efficiency for a point dipole in the presence of the rod, defined as the radiated power divided by the total emitted power (radiated power plus power lost into the rod). Emission efficiency averaged over three orthogonal dipole orientations at each of the six points as a function of rod−phosphor separation is shown in Supporting Information Figure S10, where increased quenching is observed as the separation distance is reduced. The overall PL enhancement factor is the product of the field intensity enhancement and the emission efficiency, and it is shown for each polarization in Figure 6c,d averaged over the six emitter source positions. While the PL is enhanced by up to a factor of 1.8 in the longitudinal case, only quenching is predicted for transverse polarization. To explain why a small amount of enhancement was observed experimentally for transverse polarization, we consider misorientation of the excitation laser polarization with respect to the rod axes. As shown in Supporting Information Figure S11a, rotating the transverse polarization slightly off axis changes the spatial distribution of field enhancement such that some portions of the phosphor experience amplified field intensity. As a result, the average field enhancement factor for transverse polarization can change from being less than one to greater than one with increasing misorientation angle (Supporting Information Figure S11b).

For longitudinal polarization (Figure 6d), the PL enhancement increases with decreasing rod−phosphor separation until reaching a maximum at $d = 15$ nm. Enhancement diminishes at smaller separation because of the reduction in emission efficiency due to loss in the rod. For comparison with the experimental results, the PL polarization ratio was also calculated (Figure 6e), and it displays a local maximum value of 2.3 at $d = 15$ nm. The simulated magnitudes of PL polarization ratio agree favorably with the experimental results and show that variations in the gap size from the average experimentally measured gap of 14 nm are consistent with the observed sample-to-sample differences in enhancement. The diminishing enhancement with increasing gap size is experimentally supported by PL measurement of a heterodimer with a very large gap size of 80 nm (pictured in Supporting Information Figure S12). The PL polarization ratio in this case was measured to be 1.05 ± 0.4, which is significantly closer to unity than for any of the small-gap heterodimers we reported and is comparable to the ratios measured for single phosphors having no rod nearby.

Another cause of differences in enhancement among samples is polydispersity in nanorod size, which leads to variation in the spectral position of the surface plasmon resonance. To investigate this effect, the PL enhancement was simulated as a function of rod length, with the rod−phosphor gap fixed at the maximum enhancement distance of 15 nm and the rod diameter constant at 20 nm. As seen in Supporting Information Figure S13, the PL enhancement reaches a maximum when the rod length is tuned so that the SPR matches the frequency of the 977 nm excitation. While the simulation predicts this condition to occur for a rod length of 160 nm, placing the rod in a dielectric environment (representing the SiO_2 template) rather than in free space would shift the resonance condition to a shorter rod length more closely matching the experimental length of 109 nm. Finally, we note that the condition of matching the rod resonance with the phosphor absorption can be achieved in rods of different overall sizes by simultaneously tuning the rod length and diameter. Supporting Information Figure S14 shows that for a fixed longitudinal SPR wavelength, greater enhancement can be achieved with larger-volume rods due to the greater extent of their electric field enhancement.

CONCLUSION

In summary, we have utilized template-assisted self-assembly to form nanocrystal heterodimers consisting of a single UCNP and a single Au NR and have characterized their plasmon-enhanced upconversion luminescence. Shape-selective topographical templates defined by electron-beam lithography were used to direct the coassembly of $NaYF_4$:Yb^{3+},Er^{3+} nanophosphors along with Au NRs having longitudinal SPRs tuned to match the phosphor excitation wavelength. Polarization- and power-dependent PL of individual UCNPs in the presence and absence of Au NRs was measured and simulated, and several-fold PL enhancement due to the localized electric field intensity surrounding the Au NRs was observed. The successful coassembly scheme demonstrated herein motivates extension to other material systems for achieving placement of a wide range of nanocrystal components into a variety of predesigned functional arrangements.

METHODS

Nanocrystal Synthesis. The $NaYF_4$:Yb^{3+},Er^{3+} (20%, 2%) upconversion nanophosphors[5] and the gold nanorods[85] were synthesized according to previously reported methods.

Template Fabrication and Nanocrystal Assembly. The substrate consisted of a silicon wafer with 100 nm thermal oxide (Silicon Quest International). Poly(methyl methacrylate) (PMMA) positive e-beam resist (MicroChem) was spun onto the substrate in two

layers: (1) 495 K molecular weight (MW) PMMA in anisole was spun at 3000 rpm for 45 s followed by a 4 min bake at 180 °C and then (2) 950 K MW PMMA in anisole was spun at 5000 rpm for 5 s followed by a 4 min bake at 180 °C. The thickness of the PMMA layer was ~150−200 nm as measured by atomic force microscopy (Asylum Research MFP-3D). The template pattern was written by e-beam lithography (Elionix ELS-7500EX) using a 50 kV accelerating voltage and a 50 pA beam current. The resist was developed by a 90 s immersion in a solution of methyl isobutyl ketone and isopropyl alcohol (IPA) at a 1:3 ratio and was rinsed with IPA. The e-beam pattern was transferred by etching into the silica layer using reactive ion etching (Oxford Instruments Plasmalab 80 Plus) to a depth of ~40 nm (as measured by AFM) to construct the templates. UCNPs were assembled into the template features using a "squeegee method" in which a drop of a solution of UCNPs in hexanes was dragged across the surface by a piece of PDMS cut with a razor blade from a cast sheet. The PDMS wiper was held at an angle to the substrate of ~35° and was withdrawn at ~0.8 mm/s. The PMMA layer was then removed by sonication in acetone for 30 s. A 6 nm layer of SiO_2 was deposited in a Cambridge Nanotech Savannah 200 ALD system using 3-aminopropyltriethoxysilane, O_3, and H_2O precursors. Au NRs were assembled using the apparatus described above, using a substrate withdrawal rate of 7 μm/s.

Structural and Optical Measurements. Scanning electron microscopy was performed using a JEOL 7500F HRSEM and an FEI Quanta 600 ESEM operating at 5 kV. Transmission electron microscopy was performed with a JEOL JEM-1400 TEM operating at 120 kV. Solution-phase extinction spectra of UCNPs and Au NRs were collected using a Cary 5000 UV/vis/NIR spectrometer. Spatially resolved PL measurements were taken under 977 nm illumination from a Ti:sapphire laser (Coherent, Inc. Mira HP pumped with a 532 nm 18 W Verdi diode laser). Laser power was monitored by a beam sampler and power meter (Newport 1936-C) and stabilized throughout each measurement by passing the beam through a gradient neutral density filter mounted in a motorized rotation stage (Thorlabs PRM1Z8) controlled in LabVIEW. The laser beam was coupled into a modified Olympus BX2 microscope with a short-pass dichroic mirror (Thorlabs DMSP805R) and focused by a 0.8 numerical aperture objective to a diffraction-limited (~1.5 μm diameter) spot. Samples were translated under the excitation spot with a closed-loop piezo-controlled stage (Thorlabs Nanomax) using a 200 nm step size. Upconversion luminescence was collected by a fiber and routed to a Horiba iHR 550 spectrometer with a nitrogen-cooled Symphony Si CCD camera. A short-pass filter (Newport 10SWF-950-B) at the spectrometer entrance removed any residual excitation laser signal. PL spectra were filtered using a MATLAB script to remove false signals due to cosmic ray strikes on the detector. Temperature-dependent PL spectra were collected by mounting the sample on the heating stage of an MMR Technologies D2300 optical transmission system.

Simulations. The theoretical simulations were performed using the commercial software COMSOL Multiphysics with a frequency domain solver based on the finite difference method. Only linear effects were taken into account in the simulations; therefore, the pump and the emission processes have been considered as separate phenomena and then combined together. The pump effect was simulated using plane waves with two different polarizations (parallel and orthogonal to the nanorod long axis). The emission process was studied using 6 point sources uniformly located within the phosphor, with each source modeled as three short electric dipoles oriented along *x*, *y*, and *z* with equal emission probabilities. The dispersion of the gold at the pump wavelength, as well as at the two emission wavelengths, has been taken from Palik,[86] whereas the permittivity for the phosphor was set based on Banski *et al.*[87] The simulations shown in the figures are for an emission wavelength of 540 nm; simulations performed at 650 nm displayed similar results.

Conflict of Interest: The authors declare no competing financial interest.

Acknowledgment. The authors are grateful for primary support of this work from NSF MRSEC under Award No. DMR-1120901 for Au NR assembly, AFM and SEM characterization, upgrade of the PL mapping setup, spatially resolved and polarization- and temperature-dependent PL measurements, code to filter cosmic rays and perform spectral integration, and analysis of plasmonically enhanced upconversion luminescence data. The synthesis, TEM, and extinction measurements of UCNPs and Au NRs, the design and fabrication of the templates, the deposition of UCNPs and SiO_2 using the squeegee method and ALD, respectively, and the simulations were supported by the Office of Naval Research Multidisciplinary University Research Initiative Award No. ONR-N00014-10-1-0942. Construction of the PL mapping setup was supported by the U.S. Department of Energy Office of Basic Energy Sciences, Division of Materials Science and Engineering under Award No. DE-SC0002158.

Supporting Information Available: Discussion of the modified upconversion power law. Schematic energy level diagram of the upconversion process. Additional SEM images and PL maps. PL polarization ratio integrated separately for green and red emission. Power-dependent ensemble photoluminescence measurements. Additional power-dependent PL polarization ratio data. Additional simulation details and results. This material is available free of charge *via* the Internet at http://pubs.acs.org.

Note Added after ASAP Publication: This paper published ASAP on September 5, 2014. Figure 1 was replaced and the revised version was reposted on September 9, 2014.

REFERENCES AND NOTES

1. Haase, M.; Schäfer, H. Upconverting Nanoparticles. *Angew. Chem., Int. Ed.* **2011**, *50*, 5808–5829.
2. Heer, S.; Kömpe, K.; Güdel, H.-U.; Haase, M. Highly Efficient Multicolour Upconversion Emission in Transparent Colloids of Lanthanide-Doped $NaYF_4$ Nanocrystals. *Adv. Mater.* **2004**, *16*, 2102–2105.
3. Yi, G.; Lu, H.; Zhao, S.; Ge, Y.; Yang, W.; Chen, D.; Guo, L.-H. Synthesis, Characterization, and Biological Application of Size-Controlled Nanocrystalline $NaYF_4$:Yb,Er Infrared-to-Visible Up-Conversion Phosphors. *Nano Lett.* **2004**, *4*, 2191–2196.
4. Mai, H.-X.; Zhang, Y.-W.; Si, R.; Yan, Z.-G.; Sun, L.; You, L.-P.; Yan, C.-H. High-Quality Sodium Rare-Earth Fluoride Nanocrystals: Controlled Synthesis and Optical Properties. *J. Am. Chem. Soc.* **2006**, *128*, 6426–6436.
5. Ye, X.; Collins, J. E.; Kang, Y.; Chen, J.; Chen, D. T. N.; Yodh, A. G.; Murray, C. B. Morphologically Controlled Synthesis of Colloidal Upconversion Nanophosphors and Their Shape-Directed Self-Assembly. *Proc. Natl. Acad. Sci. U.S.A.* **2010**, *107*, 22430–22435.
6. Wang, F.; Han, Y.; Lim, C. S.; Lu, Y.; Wang, J.; Xu, J.; Chen, H.; Zhang, C.; Hong, M.; Liu, X. Simultaneous Phase and Size Control of Upconversion Nanocrystals through Lanthanide Doping. *Nature* **2010**, *463*, 1061–1065.
7. Chan, E. M.; Han, G.; Goldberg, J. D.; Gargas, D. J.; Ostrowski, A. D.; Schuck, P. J.; Cohen, B. E.; Milliron, D. J. Combinatorial Discovery of Lanthanide-Doped Nanocrystals with Spectrally Pure Upconverted Emission. *Nano Lett.* **2012**, *12*, 3839–3845.
8. Gargas, D. J.; Chan, E. M.; Ostrowski, A. D.; Aloni, S.; Altoe, M. V. P.; Barnard, E. S.; Sanii, B.; Urban, J. J.; Milliron, D. J.; Cohen, B. E.; *et al.* Engineering Bright Sub-10-nm Upconverting Nanocrystals for Single-Molecule Imaging. *Nat. Nanotechnol.* **2014**, 1–6.
9. Trupke, T.; Green, M. A.; Wurfel, P. Improving Solar Cell Efficiencies by Up-Conversion of Sub-Band-Gap Light. *J. Appl. Phys.* **2002**, *92*, 4117–4122.
10. Shalav, A.; Richards, B. S.; Trupke, T.; Krämer, K. W.; Güdel, H. U. Application of $NaYF_4$:Er^{3+} Up-Converting Phosphors for Enhanced Near-Infrared Silicon Solar Cell Response. *Appl. Phys. Lett.* **2005**, *86*, 013505.
11. Van der Ende, B. M.; Aarts, L.; Meijerink, A. Lanthanide Ions as Spectral Converters for Solar Cells. *Phys. Chem. Chem. Phys.* **2009**, *11*, 11081–11095.

12. Briggs, J. A.; Atre, A. C.; Dionne, J. A. Narrow-Bandwidth Solar Upconversion: Case Studies of Existing Systems and Generalized Fundamental Limits. *J. Appl. Phys.* **2013**, *113*, 124509.
13. Lim, S. F.; Riehn, R.; Ryu, W. S.; Khanarian, N.; Tung, C.; Tank, D.; Austin, R. H. *In Vivo* and Scanning Electron Microscopy Imaging of Upconverting Nanophosphors in *Caenorhabditis elegans*. *Nano Lett.* **2006**, *6*, 169–174.
14. Nyk, M.; Kumar, R.; Ohulchanskyy, T. Y.; Bergey, E. J.; Prasad, P. N. High Contrast *In Vitro* and *In Vivo* Photoluminescence Bioimaging Using Near Infrared to Near Infrared Up-Conversion in Tm^{3+} and Yb^{3+} Doped Fluoride Nanophosphors. *Nano Lett.* **2008**, *8*, 3834–3838.
15. Chatterjee, D. K.; Rufaihah, A. J.; Zhang, Y. Upconversion Fluorescence Imaging of Cells and Small Animals Using Lanthanide Doped Nanocrystals. *Biomaterials* **2008**, *29*, 937–943.
16. Wang, F.; Banerjee, D.; Liu, Y.; Chen, X.; Liu, X. Upconversion Nanoparticles in Biological Labeling, Imaging, and Therapy. *Analyst* **2010**, *135*, 1839–1854.
17. Esipova, T. V.; Ye, X.; Collins, J. E.; Sakadžić, S.; Mandeville, E. T.; Murray, C. B.; Vinogradov, S. A. Dendritic Upconverting Nanoparticles Enable *In Vivo* Multiphoton Microscopy with Low-Power Continuous Wave Sources. *Proc. Natl. Acad. Sci. U.S.A.* **2012**, *109*, 20826–20831.
18. Milliez, J.; Rapaport, A.; Bass, M.; Cassanho, A.; Jenssen, H. P. High-Brightness White-Light Source Based on Up-Conversion Phosphors. *J. Display Technol.* **2006**, *2*, 307–311.
19. Liu, X.; Dong, G.; Qiao, Y.; Qiu, J. Transparent Colloid Containing Upconverting Nanocrystals: An Alternative Medium for Three-Dimensional Volumetric Display. *Appl. Opt.* **2008**, *47*, 6416–6421.
20. Rapaport, A.; Milliez, J.; Bass, M.; Cassanho, A.; Jenssen, H. Review of the Properties of Up-Conversion Phosphors for New Emissive Displays. *J. Display Technol.* **2006**, *2*, 68–78.
21. Boyer, J.-C.; van Veggel, F. C. J. M. Absolute Quantum Yield Measurements of Colloidal $NaYF_4$: Er^{3+},Yb^{3+} Upconverting Nanoparticles. *Nanoscale* **2010**, *2*, 1417–1419.
22. Faulkner, D. O.; Petrov, S.; Perovic, D. D.; Kherani, N. P.; Ozin, G. A. Absolute Quantum Yields in $NaYF_4$:Er,Yb Upconverters — Synthesis Temperature and Power Dependence. *J. Mater. Chem.* **2012**, *22*, 24330.
23. Liu, H.; Xu, C. T.; Lindgren, D.; Xie, H.; Thomas, D.; Gundlach, C.; Andersson-Engels, S. Balancing Power Density Based Quantum Yield Characterization of Upconverting Nanoparticles for Arbitrary Excitation Intensities. *Nanoscale* **2013**, *5*, 4770–4775.
24. Wang, F.; Liu, X. Recent Advances in the Chemistry of Lanthanide-Doped Upconversion Nanocrystals. *Chem. Soc. Rev.* **2009**, *38*, 976–989.
25. Liu, C.; Zhang, L.; Zheng, Q.; Luo, F.; Xu, Y.; Weng, W. Advances in the Surface Engineering of Upconversion Nanocrystals. *Sci. Adv. Mater.* **2012**, *4*, 1–22.
26. Qiu, P.; Zhou, N.; Chen, H.; Zhang, C.; Gao, G.; Cui, D. Recent Advances in Lanthanide-Doped Upconversion Nanomaterials: Synthesis, Nanostructures and Surface Modification. *Nanoscale* **2013**, *5*, 11512–11525.
27. Chen, G.; Yang, C.; Prasad, P. N. Nanophotonics and Nanochemistry: Controlling the Excitation Dynamics for Frequency Up- and Down-Conversion in Lanthanide-Doped Nanoparticles. *Acc. Chem. Res.* **2013**, *46*, 1474–1486.
28. Wang, F.; Deng, R.; Wang, J.; Wang, Q.; Han, Y.; Zhu, H.; Chen, X.; Liu, X. Tuning Upconversion through Energy Migration in Core−Shell Nanoparticles. *Nat. Mater.* **2011**, *10*, 968–973.
29. Wang, J.; Deng, R.; MacDonald, M. A.; Chen, B.; Yuan, J.; Wang, F.; Chi, D.; Hor, T. S. A.; Zhang, P.; Liu, G.; *et al.* Enhancing Multiphoton Upconversion through Energy Clustering at Sublattice Level. *Nat. Mater.* **2014**, *13*, 157–162.
30. Maier, S. A. *Plasmonics: Fundamentals and Applications*; Springer: New York, 2007.
31. Kulakovich, O.; Strekal, N.; Yaroshevich, A.; Maskevich, S.; Gaponenko, S.; Nabiev, I.; Woggon, U.; Artemyev, M. Enhanced Luminescence of CdSe Quantum Dots on Gold Colloids. *Nano Lett.* **2002**, *2*, 1449–1452.
32. Song, J.-H.; Atay, T.; Shi, S.; Urabe, H.; Nurmikko, A. V. Large Enhancement of Fluorescence Efficiency from CdSe/ZnS Quantum Dots Induced by Resonant Coupling to Spatially Controlled Surface Plasmons. *Nano Lett.* **2005**, *5*, 1557–1561.
33. Pompa, P. P.; Martiradonna, L.; Della Torre, A.; Della Sala, F.; Manna, L.; De Vittorio, M.; Calabi, F.; Cingolani, R.; Rinaldi, R. Metal-Enhanced Fluorescence of Colloidal Nanocrystals with Nanoscale Control. *Nat. Nanotechnol.* **2006**, *1*, 126–130.
34. Kühn, S.; Håkanson, U.; Rogobete, L.; Sandoghdar, V. Enhancement of Single-Molecule Fluorescence Using a Gold Nanoparticle as an Optical Nanoantenna. *Phys. Rev. Lett.* **2006**, *97*, 017402.
35. Kinkhabwala, A.; Yu, Z.; Fan, S.; Avlasevich, Y.; Müllen, K.; Moerner, W. E. Large Single-Molecule Fluorescence Enhancements Produced by a Bowtie Nanoantenna. *Nat. Photonics* **2009**, *3*, 654–657.
36. Anger, P.; Bharadwaj, P.; Novotny, L. Enhancement and Quenching of Single-Molecule Fluorescence. *Phys. Rev. Lett.* **2006**, *96*, 113002.
37. Saboktakin, M.; Ye, X.; Oh, S. J.; Hong, S.-H.; Fafarman, A. T.; Chettiar, U. K.; Engheta, N.; Murray, C. B.; Kagan, C. R. Metal-Enhanced Upconversion Luminescence Tunable through Metal Nanoparticle−Nanophosphor Separation. *ACS Nano* **2012**, *6*, 8758–8766.
38. Schietinger, S.; Aichele, T.; Wang, H.-Q.; Nann, T.; Benson, O. Plasmon-Enhanced Upconversion in Single $NaYF_4$:Yb^{3+}/Er^{3+} Codoped Nanocrystals. *Nano Lett.* **2010**, *10*, 134–138.
39. Feng, W.; Sun, L.-D.; Yan, C.-H. Ag Nanowires Enhanced Upconversion Emission of $NaYF_4$:Yb,Er Nanocrystals *via* a Direct Assembly Method. *Chem. Commun.* **2009**, 4393–4395.
40. Zhang, S.-Z.; Sun, L.-D.; Tian, H.; Liu, Y.; Wang, J.-F.; Yan, C.-H. Reversible Luminescence Switching of $NaYF_4$:Yb,Er Nanoparticles with Controlled Assembly of Gold Nanoparticles. *Chem. Commun.* **2009**, 2547–2549.
41. Xu, W.; Xu, S.; Zhu, Y.; Liu, T.; Bai, X.; Dong, B.; Xu, L.; Song, H. Ultra-Broad Plasma Resonance Enhanced Multicolor Emissions in an Assembled Ag/$NaYF_4$:Yb,Er Nano-Film. *Nanoscale* **2012**, *4*, 6971–6973.
42. Wawrzynczyk, D.; Bednarkiewicz, A.; Nyk, M.; Gordel, M.; Strek, W.; Samoc, M. Modulation of Up-Conversion Luminescence of Lanthanide(III) Ion Co-doped $NaYF_4$ Nanoparticles Using Gold Nanorods. *Opt. Mater.* **2012**, *34*, 1708–1712.
43. Saboktakin, M.; Ye, X.; Chettiar, U. K.; Engheta, N.; Murray, C. B.; Kagan, C. R. Plasmonic Enhancement of Nanophosphor Upconversion Luminescence in Au Nanohole Arrays. *ACS Nano* **2013**, *7*, 7186–7192.
44. Zhang, W.; Ding, F.; Chou, S. Y. Large Enhancement of Upconversion Luminescence of $NaYF_4$:Yb^{3+}/Er^{3+} Nanocrystal by 3D Plasmonic Nano-antennas. *Adv. Mater.* **2012**, *24*, OP236-41.
45. Sun, Q.-C.; Mundoor, H.; Ribot, J. C.; Singh, V.; Smalyukh, I. I.; Nagpal, P. Plasmon-Enhanced Energy Transfer for Improved Upconversion of Infrared Radiation in Doped-Lanthanide Nanocrystals. *Nano Lett.* **2014**, *14*, 101–106.
46. Paudel, H. P.; Zhong, L.; Bayat, K.; Baroughi, M. F.; Smith, S.; Lin, C.; Jiang, C.; Berry, M. T.; May, P. S. Enhancement of Near-Infrared-to-Visible Upconversion Luminescence Using Engineered Plasmonic Gold Surfaces. *J. Phys. Chem. C* **2011**, *115*, 19028–19036.
47. Paudel, H. P.; Dachhepati, D.; Bayat, K.; Mottaghian, S. S.; May, P. S.; Lin, C.; Smith, S.; Baroughi, M. F. Design, Fabrication, and Characterization of a Plasmonic Upconversion Enhancer and Its Prospects for Photovoltaics. *J. Photonics Energy* **2013**, *3*, 035598.
48. Zhang, H.; Xu, D.; Huang, Y.; Duan, X. Highly Spectral Dependent Enhancement of Upconversion Emission with Sputtered Gold Island Films. *Chem. Commun.* **2011**, *47*, 979–981.
49. Xu, W.; Zhu, Y.; Chen, X.; Wang, J.; Tao, L.; Xu, S.; Liu, T.; Song, H. A Novel Strategy for Improving Upconversion Luminescence of $NaYF_4$:Yb, Er Nanocrystals by Coupling with Hybrids of Silver Plasmon Nanostructures and Poly(methyl methacrylate) Photonic Crystals. *Nano Res.* **2013**, *6*, 795–807.

50. Zhang, C.; Lee, J. Y. Synthesis of Au Nanorod@Amine-Modified Silica@Rare-Earth Fluoride Nanodisk Core−Shell−Shell Heteronanostructures. *J. Phys. Chem. C* **2013**, *117*, 15253–15259.
51. Ge, W.; Zhang, X. R.; Liu, M.; Lei, Z. W.; Knize, R. J.; Lu, Y. Distance Dependence of Gold-Enhanced Upconversion Luminescence in Au/SiO_2/Y_2O_3:Yb^{3+},Er^{3+} Nanoparticles. *Theranostics* **2013**, *3*, 282–288.
52. Zhang, H.; Li, Y.; Ivanov, I. A.; Qu, Y.; Huang, Y.; Duan, X. Plasmonic Modulation of the Upconversion Fluorescence in $NaYF_4$:Yb/Tm Hexaplate Nanocrystals Using Gold Nanoparticles or Nanoshells. *Angew. Chem., Int. Ed.* **2010**, *49*, 2865–2868.
53. Sudheendra, L.; Ortalan, V.; Dey, S.; Browning, N. D.; Kennedy, I. M. Plasmonic Enhanced Emissions from Cubic $NaYF_4$:Yb:Er/Tm Nanophosphors. *Chem. Mater.* **2011**, *23*, 2987–2993.
54. Deng, W.; Sudheendra, L.; Zhao, J.; Fu, J.; Jin, D.; Kennedy, I. M.; Goldys, E. M. Upconversion in $NaYF_4$:Yb, Er Nanoparticles Amplified by Metal Nanostructures. *Nanotechnology* **2011**, *22*, 325604.
55. Yuan, P.; Lee, Y. H.; Gnanasammandhan, M. K.; Guan, Z.; Zhang, Y.; Xu, Q.-H. Plasmon Enhanced Upconversion Luminescence of $NaYF_4$:Yb,Er@SiO_2@Ag Core−Shell Nanocomposites for Cell Imaging. *Nanoscale* **2012**, *4*, 5132–5137.
56. Kannan, P.; Abdul Rahim, F.; Chen, R.; Teng, X.; Huang, L.; Sun, H.; Kim, D.-H. Au Nanorod Decoration on $NaYF_4$:Yb/Tm Nanoparticles for Enhanced Emission and Wavelength-Dependent Biomolecular Sensing. *ACS Appl. Mater. Interfaces* **2013**, *5*, 3508–3513.
57. Kodama, T.; Fujii, M.; Nakano, T.; Imakita, K.; Hayashi, S. Enhancement of Upconversion Luminescence of Er and Yb Co-Doped Y_2O_3 Nanoparticle by Ag Half-Shell. *Opt. Mater.* **2013**, *35*, 2394–2399.
58. Schietinger, S.; Menezes, L. D. S.; Lauritzen, B.; Benson, O. Observation of Size Dependence in Multicolor Upconversion in Single Yb^{3+}, Er^{3+} Codoped $NaYF_4$ Nanocrystals. *Nano Lett.* **2009**, *9*, 2477–2481.
59. Wu, S.; Han, G.; Milliron, D. J.; Aloni, S.; Altoe, V.; Talapin, D. V.; Cohen, B. E.; Schuck, P. J. Non-blinking and Photostable Upconverted Luminescence from Single Lanthanide-Doped Nanocrystals. *Proc. Natl. Acad. Sci. U.S.A.* **2009**, *106*, 10917–10921.
60. Ostrowski, A. D.; Chan, E. M.; Gargas, D. J.; Katz, E. M.; Han, G.; Schuck, P. J.; Milliron, D. J.; Cohen, B. E. Controlled Synthesis and Single-Particle Imaging of Bright, Sub-10 nm Lanthanide-Doped Upconverting Nanocrystals. *ACS Nano* **2012**, *6*, 2686–2692.
61. Zhao, J.; Jin, D.; Schartner, E. P.; Lu, Y.; Liu, Y.; Zvyagin, A. V.; Zhang, L.; Dawes, J. M.; Xi, P.; Piper, J. A.; *et al.* Single-Nanocrystal Sensitivity Achieved by Enhanced Upconversion Luminescence. *Nat. Nanotechnol.* **2013**, *8*, 729–734.
62. Yin, Y.; Lu, Y.; Gates, B.; Xia, Y. Template-Assisted Self-Assembly: A Practical Route to Complex Aggregates of Monodispersed Colloids with Well-Defined Sizes, Shapes, and Structures. *J. Am. Chem. Soc.* **2001**, *123*, 8718–8729.
63. Xia, Y.; Yin, Y.; Lu, Y.; McLellan, J. Template-Assisted Self-Assembly of Spherical Colloids into Complex and Controllable Structures. *Adv. Funct. Mater.* **2003**, *13*, 907–918.
64. Yin, Y.; Lu, Y.; Xia, Y. A Self-Assembly Approach to the Formation of Asymmetric Dimers from Monodispersed Spherical Colloids. *J. Am. Chem. Soc.* **2001**, *123*, 771–772.
65. Yin, Y.; Lu, Y.; Xia, Y. Assembly of Monodispersed Spherical Colloids into One-Dimensional Aggregates Characterized by Well-Controlled Structures and Lengths. *J. Mater. Chem.* **2001**, *11*, 987–989.
66. Kuemin, C.; Nowack, L.; Bozano, L.; Spencer, N. D.; Wolf, H. Oriented Assembly of Gold Nanorods on the Single-Particle Level. *Adv. Funct. Mater.* **2012**, *22*, 702–708.
67. Zhou, X.; Zhou, Y.; Ku, J. C.; Zhang, C.; Mirkin, C. A. Capillary Force-Driven, Large-Area Alignment of Multi-segmented Nanowires. *ACS Nano* **2014**, *8*, 1511–1516.
68. Yan, B.; Thubagere, A.; Premasiri, W. R.; Ziegler, L. D.; Dal Negro, L.; Reinhard, B. M. Engineered SERS Substrates with Multiscale Signal Enhancement: Nanoparticle Cluster Arrays. *ACS Nano* **2009**, *3*, 1190–1202.
69. Kraus, T.; Malaquin, L.; Schmid, H.; Riess, W.; Spencer, N. D.; Wolf, H. Nanoparticle Printing with Single-Particle Resolution. *Nat. Nanotechnol.* **2007**, *2*, 570–576.
70. Malaquin, L.; Kraus, T.; Schmid, H.; Delamarche, E.; Wolf, H. Controlled Particle Placement through Convective and Capillary Assembly. *Langmuir* **2007**, *23*, 11513–11521.
71. Holzner, F.; Kuemin, C.; Paul, P.; Hedrick, J. L.; Wolf, H.; Spencer, N. D.; Duerig, U.; Knoll, A. W. Directed Placement of Gold Nanorods Using a Removable Template for Guided Assembly. *Nano Lett.* **2011**, *11*, 3957–3962.
72. Kuemin, C.; Stutz, R.; Spencer, N. D.; Wolf, H. Precise Placement of Gold Nanorods by Capillary Assembly. *Langmuir* **2011**, *27*, 6305–6310.
73. Fan, J. A.; Bao, K.; Sun, L.; Bao, J.; Manoharan, V. N.; Nordlander, P.; Capasso, F. Plasmonic Mode Engineering with Templated Self-Assembled Nanoclusters. *Nano Lett.* **2012**, *12*, 5318–5324.
74. Henzie, J.; Andrews, S. C.; Ling, X. Y.; Li, Z.; Yang, P. Oriented Assembly of Polyhedral Plasmonic Nanoparticle Clusters. *Proc. Natl. Acad. Sci. U.S.A.* **2013**, *110*, 6640–6645.
75. Cui, Y.; Björk, M. T.; Liddle, J. A.; Sönnichsen, C.; Boussert, B.; Alivisatos, A. P. Integration of Colloidal Nanocrystals into Lithographically Patterned Devices. *Nano Lett.* **2004**, *4*, 1093–1098.
76. Chen, T.; Pourmand, M.; Feizpour, A.; Cushman, B.; Reinhard, B. M. Tailoring Plasmon Coupling in Self-Assembled One-Dimensional Au Nanoparticle Chains through Simultaneous Control of Size and Gap Separation. *J. Phys. Chem. Lett.* **2013**, *4*, 2147–2152.
77. Hong, Y.; Qiu, Y.; Chen, T.; Reinhard, B. M. Rational Assembly of Optoplasmonic Hetero-nanoparticle Arrays with Tunable Photonic-Plasmonic Resonances. *Adv. Funct. Mater.* **2014**, *24*, 739–746.
78. Giannini, V.; Fernández-Domínguez, A. I.; Heck, S. C.; Maier, S. A. Plasmonic Nanoantennas: Fundamentals and Their Use in Controlling the Radiative Properties of Nanoemitters. *Chem. Rev.* **2011**, *111*, 3888–3912.
79. Giannini, V.; Sánchez-Gil, J. A. Excitation and Emission Enhancement of Single Molecule Fluorescence through Multiple Surface-Plasmon Resonances on Metal Trimer Nanoantennas. *Opt. Lett.* **2008**, *33*, 899–901.
80. Munechika, K.; Chen, Y.; Tillack, A. F.; Kulkarni, A. P.; Plante, I. J.-L.; Munro, A. M.; Ginger, D. S. Spectral Control of Plasmonic Emission Enhancement from Quantum Dots near Single Silver Nanoprisms. *Nano Lett.* **2010**, *10*, 2598–2603.
81. Black, C. T.; Murray, C. B.; Sandstrom, R. L. Embedded Nanoparticle Films and Method for Their Formation in Selective Areas on a Surface. US 7,682,591 B2, 2010.
82. Ming, T.; Zhao, L.; Yang, Z.; Chen, H.; Sun, L.; Wang, J.; Yan, C. Strong Polarization Dependence of Plasmon-Enhanced Fluorescence on Single Gold Nanorods. *Nano Lett.* **2009**, *9*, 3896–3903.
83. Pollnau, M.; Gamelin, D.; Lüthi, S.; Güdel, H.; Hehlen, M. Power Dependence of Upconversion Luminescence in Lanthanide and Transition-Metal-Ion Systems. *Phys. Rev. B* **2000**, *61*, 3337–3346.
84. Suyver, J.; Aebischer, A.; García-Revilla, S.; Gerner, P.; Güdel, H. Anomalous Power Dependence of Sensitized Upconversion Luminescence. *Phys. Rev. B* **2005**, *71*, 125123.
85. Ye, X.; Zheng, C.; Chen, J.; Gao, Y.; Murray, C. B. Using Binary Surfactant Mixtures To Simultaneously Improve the Dimensional Tunability and Monodispersity in the Seeded Growth of Gold Nanorods. *Nano Lett.* **2013**, *13*, 765–771.
86. Palik, E. D. *Handbook of Optical Constants of Solids*; Academic Press: Boston, MA, 1985.
87. Banski, M.; Afzaal, M.; Podhorodecki, A.; Misiewicz, J.; Abdelhady, A. L.; O'Brien, P. Passivation of Lanthanide Surface Sites in Sub-10 nm $NaYF_4$:Eu^{3+} Nanocrystals. *J. Nanopart. Res.* **2012**, *14*, 1228.